14th International Symposium on Turbulence and Shear Flow Phenomena (TSFP14)
Heidelberg, Germany, July 28–31, 2026

IMPACT OF COALESCENCE MODELLING ON TURBULENCE STATISTICS IN MULTIPHASE FLOW SIMULATIONS

Jordi Poblador-Ibanez
Department of Maritime and Transport Technology
Delft University of Technology
Mekelweg 2, Delft, 2628 CD, The Netherlands
J.PobladorIbanez@tudelft.nl

Bendiks Jan Boersma
Department of Maritime and Transport Technology
Delft University of Technology
Mekelweg 2, Delft, 2628 CD, The Netherlands
B.J.Boersma@tudelft.nl

ABSTRACT

This study investigates how various numerical methodologies for preventing numerical bubble coalescence impact the accuracy of turbulence statistics in high-fidelity simulations of turbulent channel bubbly flows. The results demonstrate that the turbulence statistics are highly sensitive to the specific approaches integrated within each flow solver. In particular, the inclusion of a repulsive force between bubbles in the momentum equation to prevent numerical coalescence instead of a multiple-markers approach reveals modelling challenges. We show that the impact on turbulence statistics is small, but not negligible, for total void fractions up to 2.4%. Additionally, the repulsive force might induce flow asymmetries if not sufficiently localized.

INTRODUCTION

Bubbly flows are ubiquitous in the energy transition (e.g., coolant boiling in heat exchangers or hydrogen bubbles in electrolysis). Numerical studies are essential to improve their understanding and enable new technologies. However, practical systems are laden with multiple bubbles and involve a very wide range of length scales. For example, bubble coalescence is a physical process that occurs on the nanoscale (Tryggvason *et al.*, 2013). This multi-scale nature limits the usability of high-fidelity multiphase solvers since computations can become prohibitively expensive. Consequently, most studies analyse canonical turbulent flows that preserve key bubble-dispersion physics, such as turbulent channel bubbly flows. Here, we consider this configuration and discuss how modelling choices affect turbulence statistics, emphasizing the need for thorough validation across published numerical data.

"Ground-truth" turbulence statistics may be obtained from high-fidelity simulations with advanced multiphase solvers (Cifani *et al.*, 2020; Nemati *et al.*, 2021). Experimental studies of such flows are scarce, and only limited data on mean profiles and fluctuations exist (Pang & Wei, 2013). In contrast, simulations offer greater insight since flow information is directly accessible. Yet, multiple numerical approaches are available (Elghobashi, 2019), and one must carefully assess whether the physics are affected by the chosen methodologies.

Nemati *et al.* (2021) reproduced the statistics of turbulent channel bubbly flows in downflow and upflow conditions, consistent with Lu & Tryggvason (2006) and Dabiri *et al.* (2013). They employed a one-fluid Navier-Stokes formulation with the Coupled Level-Set Volume-of-Fluid (CLSVOF) method and multiple markers to prevent numerical coalescence of the bubbles, whereas the reference studies used a similar approach with the Front-Tracking method. Nonetheless, some differences, particularly for the velocity fluctuations, were attributed to the discretization methods and grid resolution.

Arguably, a multiphase solver such as that from Nemati *et al.* (2021) combines the best techniques available. However, such approaches come at a great computational cost as the domain size and number of bubbles increase. This raises the question of whether simpler, cheaper solvers can reproduce the same turbulence statistics. This is explored by using a one-fluid formulation of the Navier-Stokes equations coupled to a geometric Volume-of-Fluid (VOF) framework. Instead of individual markers, a repulsive force is implemented in the liquid phase to ensure that the bubbles do not coalesce.

METHODOLOGY

This section summarizes the incompressible high-fidelity multiphase flow solver used in this work. For more details, the reader is referred to Poblador-Ibanez *et al.* (2025).

A geometric VOF method is used based on the local reconstruction of the interface at each cell. The interface orientation and cut volumes are obtained from a Piecewise Linear Interface Construction (PLIC) where the normal unit vector $\mathbf{n}_\Gamma$ and curvature κ are obtained, respectively, from the Mixed-Youngs-Centre (Aulisa *et al.*, 2007) and Height Function (López & Hernández, 2010; Baraldi *et al.*, 2014) methods. The interface is advected using the conservative three-step split advection scheme from Sussman & Puckett (2000).

The one-fluid Navier-Stokes equations for incompressible two-phase flows are the continuity and momentum equations, expressed as

$$\nabla \cdot \mathbf{u} = 0 \tag{1}$$

$$\rho \left(\frac{\partial \mathbf{u}}{\partial t} + \nabla \cdot (\mathbf{u} \otimes \mathbf{u}) \right) = -\nabla p + \nabla \cdot \mathbf{T} + \rho \mathbf{g} + \mathbf{f}_\sigma + \mathbf{f}_R \tag{2}$$

where $\mathbf{u}$ is the one-fluid velocity, p the pressure, $\mathbf{g}$ the gravity acceleration, $\mathbf{T} = \mu(\nabla \mathbf{u} + \nabla \mathbf{u}^T)$ the viscous stress tensor, and ρ and μ the volume-averaged density and viscosity using the liquid volume fraction C, e.g., $\rho = \rho_L C + \rho_G (1-C)$. The subscripts L and G refer to the liquid and gas phases, respectively. The equations are discretized using second-order central differences, except for the convective term in Eq. (2) which is discretized using the SMART scheme (Gaskell & Lau, 1988). A second-order Adams-Bashforth scheme is used for the temporal integration, and a predictor-projection approach coupled to the split pressure gradient method by Cifani (2019) is implemented. Thus, a direct pressure solver imposes the divergence-free condition to machine-error precision.

Surface tension $\mathbf{f}_\sigma = -\sigma\kappa\mathbf{n}_\Gamma\delta_\Gamma$ is discretized using the Continuum Surface Force model (Brackbill *et al.*, 1992), where σ is the surface tension coefficient, and δ_Γ a Dirac delta function active only across the interface. $\mathbf{f}_R$ is a repulsive force to prevent numerical bubble coalescence. The use of $\mathbf{f}_R$ has been proposed as an alternative to tracking individual markers since it is easier to implement and adds minimal computational overhead. Here, $\mathbf{f}_R$ is given by Eq. (3) following De Vita *et al.* (2019). R is the initial bubble radius and U the mean bulk velocity of the equivalent single-phase channel flow with same $Re_\tau = u_\tau\delta\nu_L^{-1}$. δ is the channel half-thickness, u_τ the wall friction velocity, and ν_L the liquid's kinematic viscosity. Ψ is the distance function from the interface (see De Vita *et al.* (2019) for VOF implementation), and a and b are constants to be determined. $\mathbf{f}_R$ is computed at cell centres in liquid cells within bubble conflict regions, then averaged at staggered locations. A conflict region is defined when two bubbles are detected within a 7x7x7 stencil around the cell. However, the additional body force affects flow development, as depicted by the velocity field between bubbles in Figure 1, which requires a thorough evaluation of its impact on turbulence statistics.

$$\mathbf{f}_R = \mu_L R U\left(\frac{a}{\Psi}+\frac{b}{\Psi^2}\right)\mathbf{n}_\Gamma \tag{3}$$

RESULTS

A vertical channel in downflow conditions defined by $\delta =$ 5 mm and size $L_x = 2\delta$ (wall-normal), $L_y = 13\delta$ (streamwise) and $L_z = 5\delta$ (spanwise) is considered. Cases with a total void fraction of $\alpha = 1.2\%$ and $\alpha = 2.4\%$ are chosen from Nemati *et al.* (2021) with an initial bubble diameter of $D_b = 1.6909$ mm (L48 and H96, respectively). A uniform mesh is used with 128 or 256 cells in the wall-normal direction, resulting in a $x_w^+ = 1.4$ or $x_w^+ = 0.7$ for $Re_\tau = 180$, respectively, to ensure the turbulence scales are resolved. This translates to a bubble resolution of about 21 cells per diameter in the coarse case and 42 cells per diameter in the fine case, which is enough to capture the bubble dynamics in a VOF framework. Additional parameters of the problem are given by $\rho_L = 603.52$ kg/m^3, $\rho_G = 6.0352$ kg/m^3, $\mu_L = 69.403$ μPa·s, $\mu_G = 1.2493$ μPa·s, $We = \rho_L u_\tau^2\delta\sigma^{-1} = 8.8767\times10^{-2}$, $Fr = u_\tau^2|g|^{-1}\delta^{-1} = 2.6422\times10^{-2}$ and $Eo = (\rho_L-\rho_G)|g|D_b^2\sigma^{-1} = 0.3804$. With such flow parameters, the bubbles are slightly deformable and may not remain spherical, as shown by the Eötvös number Eo. The down flow is driven by gravity and a mean pressure gradient in the streamwise direction (Nemati *et al.*, 2021), as shown in Eq. (4), where the shear stress at the wall is $\tau_w = \rho_L u_\tau^2$, ρ_{avg} is the volume-averaged density in the computational domain and g_y is the signed gravity component in the streamwise direction.

$$\frac{dp_0}{dy} = \frac{\tau_w}{\delta} + \rho_{avg} g_y \tag{4}$$

The solver is validated against the single-phase turbulent channel from Moser *et al.* (1999) for $Re_\tau = 180$. Figure 2 shows the mean streamwise velocity and the root mean square (rms) of the velocity fluctuations. First- and second-order statistics of the turbulent flow are well captured, even with the coarse mesh. The implementation of the SMART scheme has a negligible impact in the single-phase case despite the additional numerical dissipation compared to pure central differences. In multiphase solvers using geometric VOF, dissipative schemes can be necessary due to the existing spurious currents around the interface, which can quickly destabilize the solution if central differences are used.

The values of a and b to prevent the numerical coalescence of the bubbles are found via a trial and error approach since a and b depend, among other factors, on the grid resolution. Here, $a = 1\times10^6$ m^{-2} for $x_w^+ = 1.4$, and $a = 2\times10^6$ m^{-2} for $x_w^+ = 0.7$. The constant b is given by $a/b = 15.714$ m^{-1} (De Vita *et al.*, 2019). Lastly, the spherical bubbles with D_b are initialized by inserting them into a snapshot of the fully-developed single-phase turbulent channel flow in an array $N_x \times N_y \times N_z$, uniformly distributed in each direction. For $\alpha = 1.2\%$, the array is 2×13×3, and for $\alpha = 2.4\%$ it is 3×13×4. The movement of the bubbles rapidly randomizes and, after five flow-through times, the collection of the statistics of the turbulent channel bubbly flow starts. These are collected for about ten flow-through-times after showing sufficient temporal convergence. The velocity components are Favre averaged (decomposed as $u_i = \tilde{u}_i + u_i''$, where $\tilde{u}_i = \overline{\rho u_i}/\overline{\rho}$) and all other variables are Reynolds averaged (decomposed as, e.g., $\rho = \overline{\rho} + \rho'$).

Reasonable agreement of first- and second-order velocity statistics against Nemati *et al.* (2021) is observed in Figure 3, suggesting that a repulsive force can produce turbulence statistics similar to a multiple markers formulation. Note that Figure 3b shows a Reynolds-averaged streamwise velocity weighted by the volume fraction C as a measure of the mean liquid streamwise velocity following Lu & Tryggvason (2006); Nemati *et al.* (2021).

Yet, compared to the single-phase channel, the results highly depend on the bubble resolution and flow symmetry is lost. This could be attributed to a combination of various factors in our solver. Namely coarser bubble resolutions enhance the spurious currents from the geometric VOF and the repulsive force may induce sharp velocity gradients in between bubbles to prevent coalescence. The interaction between these effects, the inconsistent mass-momentum advection in our multiphase formulation, and the asymmetries introduced by the SMART scheme balancing numerical diffusion can easily affect the flow development. This is supported by the fact that mesh refinement improves flow symmetry. Figure 4 shows the mean void fraction across the channel for both α cases and the rms of the density fluctuations for $\alpha = 1.2\%$. With mesh refinement, the clustering of bubbles around the channel centre is more symmetric, as expected for downflow conditions. Next, Figure 5 depicts the mean repulsive force along the wall-normal, streamwise and spanwise directions. For finer grids, lower force magnitudes are generally observed. That is, the force is less active in the flow since finer grids result in fewer conflict regions between bubbles.

Beyond flow symmetry issues, Figure 5 highlights the stochastic nature of $\mathbf{f}_R$, randomly fluctuating around zero. This reinforces the idea that $\mathbf{f}_R$ can indeed be used to prevent numerical coalescence without modifying expected flow patterns when properly discretized and resolved at a cheaper computational cost than a multiple markers formulation. However, the repulsive force has additional caveats that need to be properly analysed.

The modified flow field between conflicting bubbles may affect the velocity statistics, particularly second-order statistics such as the velocity fluctuations. Indeed, Figures 3c and 3d show nearly excellent agreement with Nemati *et al.* (2021) near the walls, but differences are greater near the centre of the channel where bubbles accumulate. One would expect the effects of $\mathbf{f}_R$ to average out over time, but this has not been observed in, e.g., the mean repulsive force components in Figure 5 during the statistics collection time. Thus, the repulsive force may induce a net forcing effect in the flow. Despite each component fluctuating around a zero value across the channel, the net effect on each direction, calculated by integrating the curves in Figure 5 along x^+, is not zero (see Table 1). However, mesh refinement helps decrease the net effect of $\mathbf{f}_R$ substantially, with some force components decreasing up to an order of magnitude between a resolution given by $x_w^+ = 1.4$ and a resolution given by $x_w^+ = 0.7$.

Table 1: Net repulsive force in [N/m^3] obtained by integrating the curves in Figure 5.

Case	$\overline{f}_{R_x}$	$\overline{f}_{R_y}$	$\overline{f}_{R_z}$
$\alpha = 1.2\%, x_w^+ = 1.4$	0.8399	-0.9438	0.9184
$\alpha = 1.2\%, x_w^+ = 0.7$	-0.2430	-0.0275	0.3828
$\alpha = 2.4\%, x_w^+ = 1.4$	1.5519	-3.7560	0.8828
$\alpha = 2.4\%, x_w^+ = 0.7$	-0.1880	-0.2920	0.4248

The magnitudes of $\mathbf{f}_R$ shown in Figure 5 or Table 1 are indeed much smaller than the driving forces in the channel, but they can still be responsible for introducing asymmetries in the flow, especially along the wall-normal or spanwise directions. To contextualize this, Figure 6a shows the distribution of the mean body forces including the driving pressure gradient $\frac{dp_0}{dy}$ and gravity, which only act in the streamwise direction. In general, the combined effect can be locally one to two orders of magnitude greater than $\mathbf{f}_R$. Note that in this one-fluid formulation, an additional body force exists, i.e., surface tension. However, a similar analysis of $\mathbf{f}_\sigma$ is out of scope of this paper.

Lastly, the impact of $\mathbf{f}_R$ in the context of turbulent kinetic energy (TKE) production is analysed. By looking at the equation for the Favre averaged TKE, $k = \frac{1}{2}\widetilde{u_i''u_i''}$, specific TKE production terms characteristic of bubbly flows (or buoyant flows) are identified (Nemati *et al.*, 2021), i.e., $-\overline{\rho}\overline{u_y''}g_y$. This term is shown in Figure 6b showcasing how the relative movement of bubbles across the carrier phase is responsible for TKE production around the centre of the channel. Thus, the larger velocity fluctuations reported in Figures 3c and 3d compared to the single-phase channel flow. Note that the effects of flow asymmetries are even more pronounced here.

Similarly, one can derive the repulsive force production term, given by $\overline{u_i'' f_{R_i}'}$. Here, and for k, Einstein summation convention is used. The repulsive force TKE production is shown in Figure 6c and, as expected, its influence region is around the channel centre where bubbles cluster and the repulsive force is active. The contribution to TKE is not negligible and of similar magnitude as the buoyancy production term, especially for $\alpha = 2.4\%$ where a higher concentration of bubbles exists. With mesh refinement, the TKE production associated with $\mathbf{f}_R$ decreases. This observation partially explains the differences in the velocity fluctuations reported in Figures 3c and 3d with respect to the reference data from Nemati *et al.* (2021) and shows that, despite the computationally friendlier setup of handling bubble coalescence with a repulsive force, a cost is paid in terms of capturing the correct turbulence statistics if $\mathbf{f}_R$ is predominantly active in the flow.

CONCLUSIONS

This work has implemented a repulsive force formulation to prevent bubble coalescence in a bubbly turbulent channel flow in downflow conditions. The turbulence statistics have been validated against a previous numerical work based on a multiple markers approach where coalescence is prevented by tracking each bubble individually. While optimized workflows exist to handle multiple markers, the framework still suffers from additional computational overhead compared to adding a new body force in the Navier-Stokes equation.

While the validation is quantitatively successful, the repulsive force may enhance flow asymmetries when coupled with the particular numerical modelling approach. We show that the repulsive force net effect is not negligible in terms of driving the flow in the streamwise, wall-normal and spanwise directions. Moreover, the repulsive force contributes to producing turbulent kinetic energy around the cluster of bubbles. Thus, partially explaining the differences in velocity fluctuations near the centre of the channel between our work and the reference data. As expected, these perturbations on the flow development vanish as the mesh is refined.

The analysis of the impact of the repulsive force on the turbulent flow motivates the need to improve such modelling frameworks in future work. For example, removing the constraint related to tuning the model's coefficients or identifying pathways whereby directionality is embedded in the formulation, i.e., whether two conflicting bubbles are actually on a collision path. These could be explored to minimize the activation of $\mathbf{f}_R$ in the flow and the impact on turbulence statistics. Moreover, the integration of the repulsive force with scalings derived from film drainage theory could allow certain physics-based control on the bubble coalescence phenomena, i.e., tuning the force magnitude to ensure bubbles bounce or merge according to drainage time scales.

ACKNOWLEDGMENTS

This publication is part of the project *Bridging Scales in Bubbly Flow Simulations with Phase Transition* with file number 21848 of the research programme *NWO Talent Program Veni TTW 2024* which is (partly) financed by the Dutch Research Council (NWO) under the grant https://doi.org/10.61686/TNVLQ16996. Additionally, this publication is also part of the Small Compute projects *Development of High-Fidelity Multiphase Solver for Boiling Flows* and *Coupling of Interfacial Sub-grid Models in High-Fidelity Multiphase Solvers* of the research programme *Computing Time on National Computer Facilities* which is (partly) financed by the Dutch Research Council (NWO).

This work used the Dutch national e-infrastructure with the support of the SURF Cooperative using grant no. EINF-9679 and grant no. EINF-16431. The authors also acknowledge the use of computational resources of DelftBlue supercomputer, provided by Delft High Performance Computing Centre (https://www.tudelft.nl/dhpc).

REFERENCES

Aulisa, E., Manservisi, S., Scardovelli, R. & Zaleski, S. 2007 Interface reconstruction with least-squares fit and split advection in three-dimensional cartesian geometry. *Journal of Computational Physics* **225** (2), 2301–2319.

Baraldi, A., Dodd, M.S. & Ferrante, A. 2014 A mass-conserving volume-of-fluid method: Volume tracking and droplet surface-tension in incompressible isotropic turbulence. *Computers & Fluids* **96**, 322–337.

Brackbill, J.U, Kothe, D.B & Zemach, C. 1992 A continuum method for modeling surface tension. *Journal of Computational Physics* **100** (2), 335–354.

Cifani, P. 2019 Analysis of a constant-coefficient pressure equation method for fast computations of two-phase flows at high density ratios. *Journal of Computational Physics* **398**, 108904.

Cifani, P., Kuerten, J.G.M. & Geurts, B.J. 2020 Flow and bubble statistics of turbulent bubble-laden downflow channel. *International Journal of Multiphase Flow* **126**, 103244.

Dabiri, S., Lu, J. & Tryggvason, G. 2013 Transition between regimes of a vertical channel bubbly upflow due to bubble deformability. *Physics of Fluids* **25** (10), 102110.

De Vita, F., Rosti, M.E., Caserta, S. & Brandt, L. 2019 On the effect of coalescence on the rheology of emulsions. *Journal of Fluid Mechanics* **880**, 969–991.

Elghobashi, S. 2019 Direct numerical simulation of turbulent flows laden with droplets or bubbles. *Annual Review of Fluid Mechanics* **51** (Volume 51, 2019), 217–244.

Gaskell, P.H. & Lau, A.K.C. 1988 Curvature-compensated convective transport: SMART, a new boundedness-preserving transport algorithm. *International Journal for Numerical Methods in Fluids* **8** (6), 617–641.

Lu, J. & Tryggvason, G. 2006 Numerical study of turbulent bubbly downflows in a vertical channel. *Physics of Fluids* **18** (10), 103302.

López, J. & Hernández, J. 2010 On reducing interface curvature computation errors in the height function technique. *Journal of Computational Physics* **229** (13), 4855–4868.

Moser, R.D., Kim, J. & Mansour, N.N. 1999 Direct numerical simulation of turbulent channel flow up to Re$_\tau$=590. *Physics of Fluids* **11** (4), 943–945.

Nemati, H., Breugem, W.-P., Kwakkel, M. & Boersma, B.J. 2021 Direct numerical simulation of turbulent bubbly down flow using an efficient CLSVOF method. *International Journal of Multiphase Flow* **135**, 103500.

Pang, M. & Wei, J. 2013 Experimental investigation on the turbulence channel flow laden with small bubbles by PIV. *Chemical Engineering Science* **94**, 302–315.

Poblador-Ibanez, J., Valle, N. & Boersma, B.J. 2025 A momentum balance correction to the non-conservative one-fluid formulation in boiling flows using volume-of-fluid. *Journal of Computational Physics* **524**, 113704.

Sussman, M. & Puckett, E.G. 2000 A coupled level set and volume-of-fluid method for computing 3D and axisymmetric incompressible two-phase flows. *Journal of Computational Physics* **162** (2), 301–337.

Tryggvason, G., Dabiri, S., Aboulhasanzadeh, B. & Lu, J. 2013 Multiscale considerations in direct numerical simulations of multiphase flows. *Physics of Fluids* **25** (3), 031302.

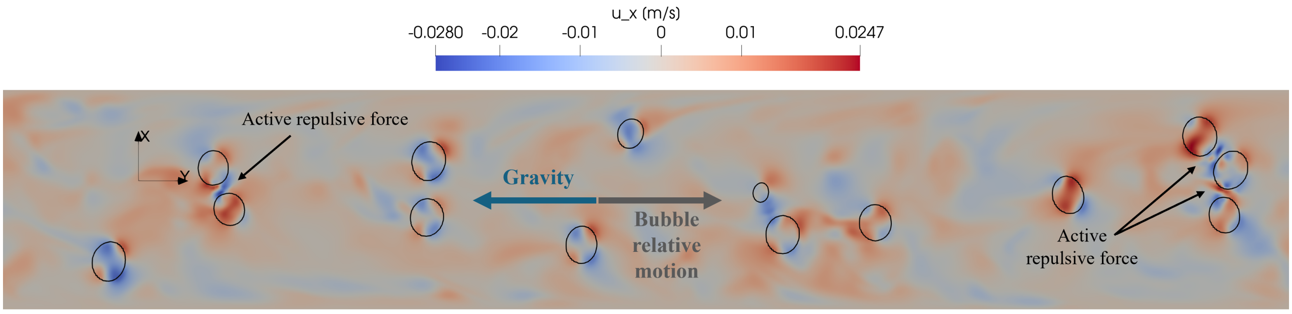

Figure 1: Snapshot of wall-normal velocities on an *xy*-slice of the turbulent channel bubbly flow with $Re_\tau = 180$ and $\alpha = 2.4\%$. The black iso-contours represent the bubble's interface where $C = 0.5$.

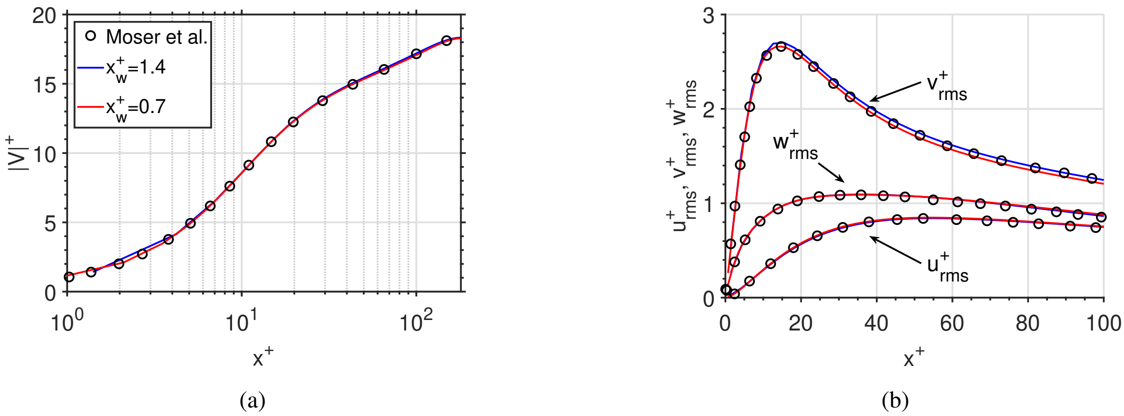

Figure 2: Validation of the single-phase turbulent channel flow with $Re_\tau = 180$ against data from Moser *et al.* (1999). (a) mean streamwise velocity; (b) root mean square (rms) of velocity fluctuations. The velocities are non-dimensionalized by u_τ.

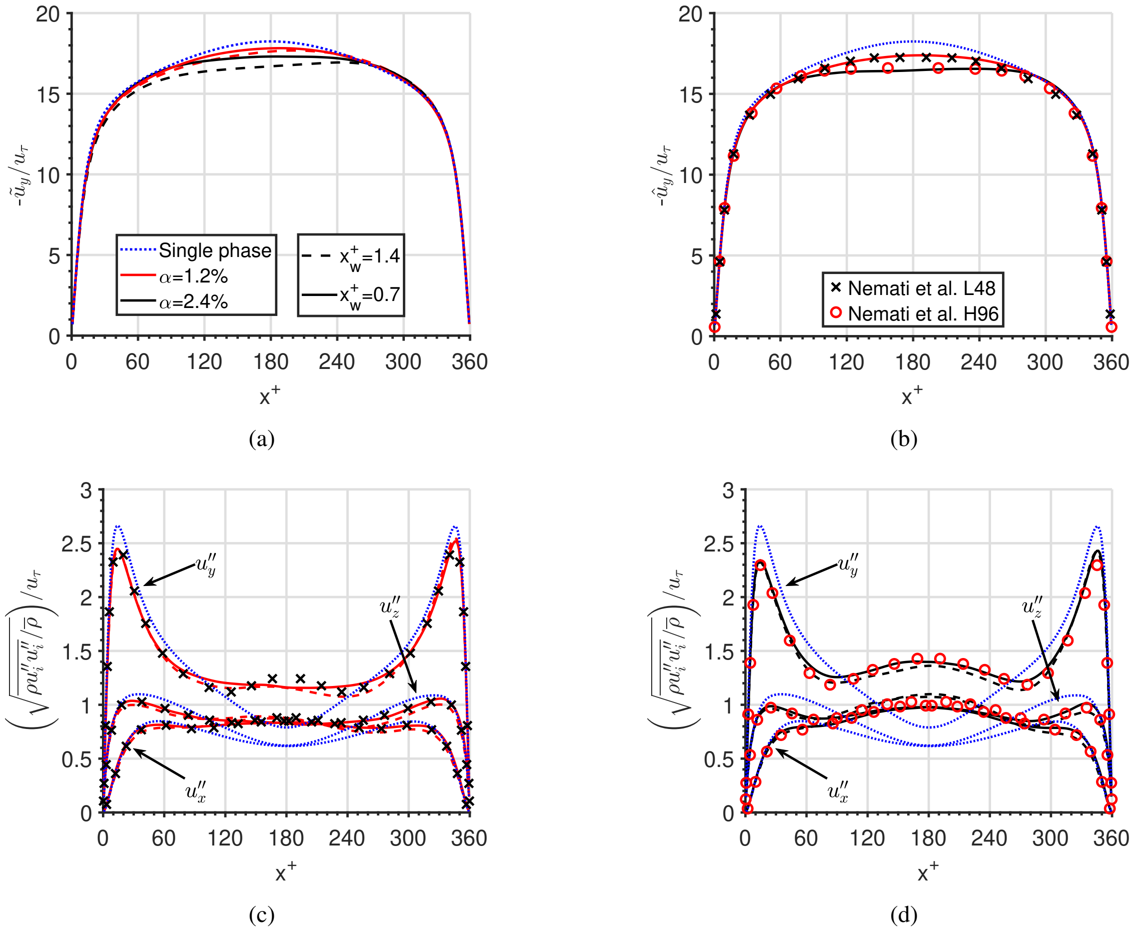

Figure 3: Turbulent channel bubbly flow with $Re_\tau = 180$ compared against Nemati *et al.* (2021) for total void fractions of $\alpha = 1.2\%$ and $\alpha = 2.4\%$. The velocities are non-dimensionalized by u_τ. (a) mean streamwise velocity; (b) mean streamwise velocity weighted by the volume fraction C; (c) rms of velocity fluctuations for $\alpha = 1.2\%$; (d) rms of velocity fluctuations for $\alpha = 2.4\%$.

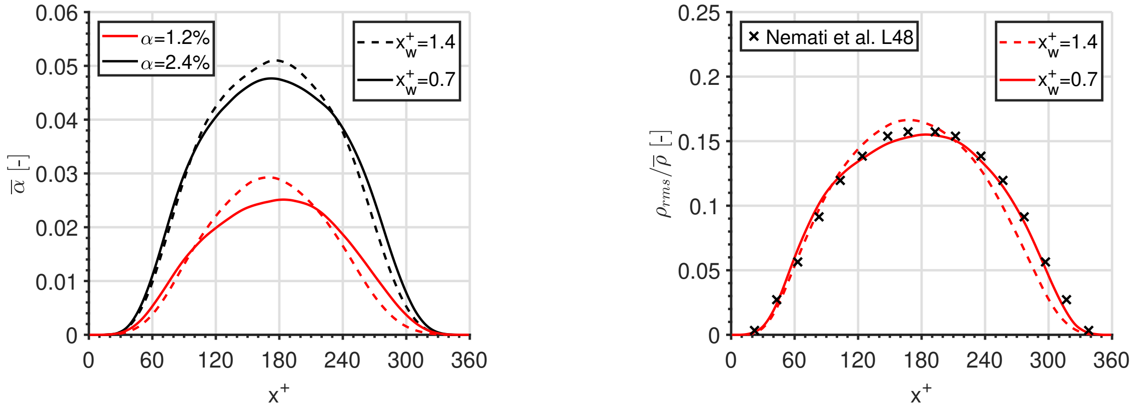

(a) (b)

Figure 4: Turbulent channel bubbly flow with $Re_\tau = 180$ compared against Nemati *et al.* (2021) for total void fractions of $\alpha = 1.2\%$ and $\alpha = 2.4\%$. (a) mean void fraction; (b) rms of density fluctuations normalized by the mean density for $\alpha = 1.2\%$.

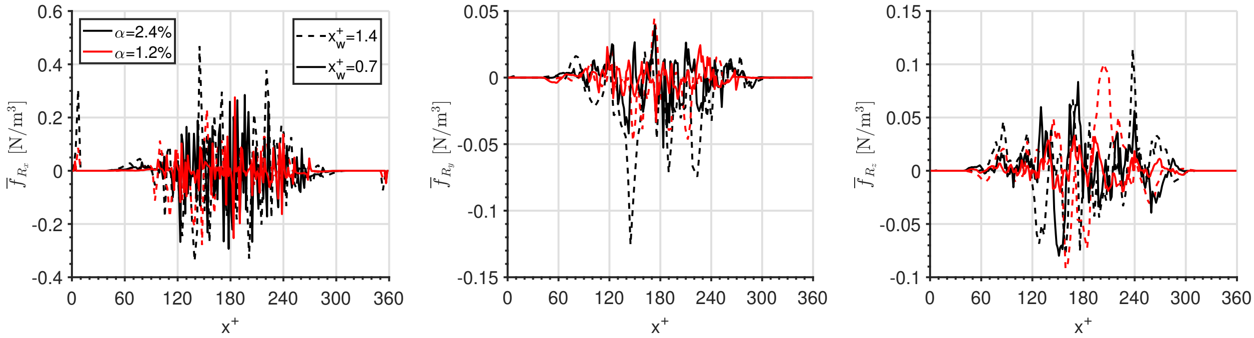

(a) (b) (c)

Figure 5: Mean repulsive force in the turbulent channel bubbly flow with $Re_\tau = 180$ for total void fractions of $\alpha = 1.2\%$ and $\alpha = 2.4\%$. (a) mean wall-normal component; (b) mean streamwise component; (c) mean spanwise component.

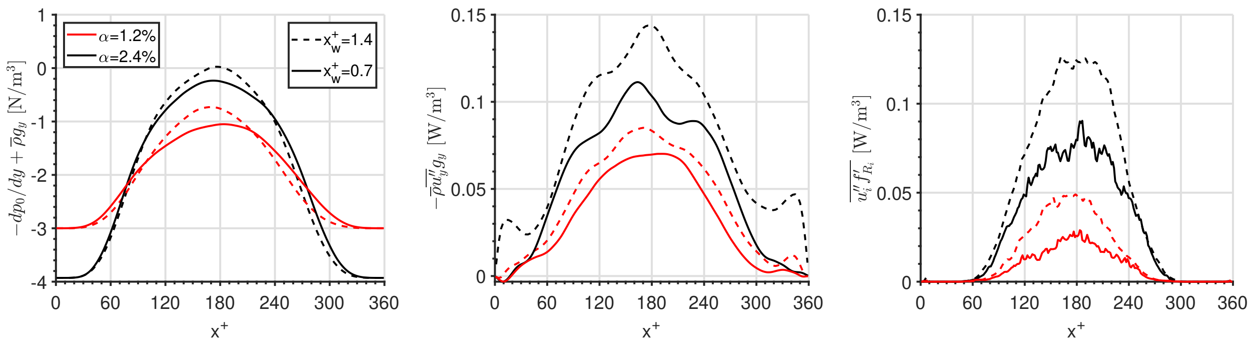

(a) (b) (c)

Figure 6: Characteristics of the turbulent channel bubbly flow with $Re_\tau = 180$ for total void fractions of $\alpha = 1.2\%$ and $\alpha = 2.4\%$. (a) mean driving force in the streamwise direction; (b) buoyancy TKE production term; (c) repulsive force TKE production term.